AIAA JOURNAL
Vol. 48, No. 4, April 2010

Aeroelastic-Acoustics Simulation of Flight Systems

K. K. Gupta*
NASA Dryden Flight Research Center, Edwards, California 93523
S. B. Choi†
Advanced Engineering Solutions, Inc., Ormond Beach, Florida 32174
and
A. Ibrahim‡
Norfolk State University, Norfolk, Virginia 23504

DOI: 10.2514/1.44098

This paper describes the details of a novel numerical finite-element-based analysis procedure and a resulting code for the simulation of the acoustics phenomenon arising from aeroelastic interactions. Both computational fluid dynamics and structural simulations are based on finite element discretization employing unstructured grids. The sound pressure level on structural surfaces is calculated from the root mean square of the unsteady pressure, and the acoustic-wave frequencies are computed from a fast Fourier transform of the unsteady pressure distribution as a function of time. The newly developed tool proves to be unique, as it is designed to analyze complex practical problems involving computations in a routine fashion.

I. Introduction

MANY practical flight vehicles are often characterized by complex interactions among a number of primary disciplines such as structures, fluids, controls, and propulsion, among others. In some critical flight regimes, such as transonic flow, the dynamic behavior of fluids tends to be highly complex, needing computational fluid dynamics (CFD)-based modeling, rather than linear aerodynamic methods, for accurate prediction of unsteady flow. Such unsteady pressure values, generated by the interaction of fluids and elastic structures, could then be conveniently used to compute acoustic-wave frequencies and sound pressure levels (in decibels).

For accurate simulation of complex engineering problems pertaining to advanced aircraft, it is necessary to employ unstructured grids to model the fluids discipline, as in the case for structures modeling. Effective CFD-based aeroelastic (AE) modeling using finite element (FE) discretization of both fluids and structures and employing unstructured grids has been effectively used for simulation of Hyper-X [1,2] and F-18 [3,4] aircraft. In connection with a current ongoing project, Stratospheric Observatory for Infrared Astronomy (SOFIA) [5], evaluation of acoustic activities in the large open cavity of the modified Boeing 747SP aircraft housing the 2.7 m infrared telescope became a crucial issue. Observations will be made at a nominal cruise condition of Mach 0.84 at altitudes between 39,000 and 45,000 ft. Acoustic analyses [6,7] have shown the potential for resonances within the cavity during flight. These partial-open-door analyses concluded that flight-test data are needed to reduce uncertainties. It is essential then that the cavity acoustics are monitored during the cavity-door-open flight-test phase to detect and avoid encountering acoustic resonances of the cavity.

There are uncertainties associated with the acoustic analyses performed so far, as they do not consider the effect of interaction with the flexible structure. Thus, in support of the SOFIA project, the multidisciplinary analysis code STARS [8] was recently extended to include the acoustic effects and takes into account the effect of structural flexibility. Such an aeroelastic-acoustics analysis involving structures, CFD steady and unsteady flows, fluid–structural interactions, and resulting evaluation of acoustic activities is described herein in some detail. The current simulation methodology effects the simultaneous time integration of the structural equations of motion with the governing flow equations for the computation of unsteady aerodynamic forces. In these time-marching unsteady flow and aeroelastic calculations, the aerodynamic mesh needs to be updated at every time level, particularly for large structural deformations, so that it follows the deformed structural configuration. However, considering the time required to generate a single domain mesh for a flow solution, rediscretization of the computational domain at each time step appears to be rather impractical.

The number of calculations can be substantially reduced if the surface deformation can be simulated without having to update the aerodynamic mesh. This may be achieved by applying a transpiration boundary condition [9–11] at the surface nodal points. In this process, the body normals are rotated in the same directions as they would be in the actual deflected shape, thus leaving the original aerodynamic mesh unaffected throughout the aeroelastic stability investigation. This procedure works rather well, particularly for small deformation problems [11].

In this paper, the common finite element idealization is effected for both fluids and structures continua. Adoption of the transpiration method enables the original aerodynamic mesh to remain unchanged during the entire analysis process. A CFD-based aeroelastic analysis is effected first, and the resulting unsteady pressure solutions are next used to compute the acoustic effects. This is followed first by a set of numerical results of aeroelastic simulation for a 2-D airfoil, and such results are verified with known analytical solutions. Aeroelastic-acoustic simulation results are next presented for a 3-D cantilever wing [8] with a NACA 0012 airfoil, which involves calculation of sound pressure levels as well as acoustic-wave frequencies.

The resulting code proves to be unique, as it enables effective solution of complex practical problems in an efficient fashion using modest computing resources. Employment of the common FE technique for both fluids and structures also ensures accurate interaction of the two disciplines, which is not available in other existing similar codes.

II. Numerical Formulation: Time-Marched Aeroelastic-Acoustics Simulation

For the nonlinear aeroelastic analyses [2,4], both the fluids and structures domains are idealized by the finite element method using unstructured grids. This process yields the unsteady pressure

Presented as paper 39 at the 47th AIAA Aerospace Sciences Meeting, Orlando, FL, 5–8 January 2009; received 4 March 2009; revision received 1 December 2009; accepted for publication 4 December 2009.

*Research Engineering Directorate. Associate Fellow AIAA.
†Research Engineer. Member AIAA.
‡Professor, Department of Engineering. Member AIAA.

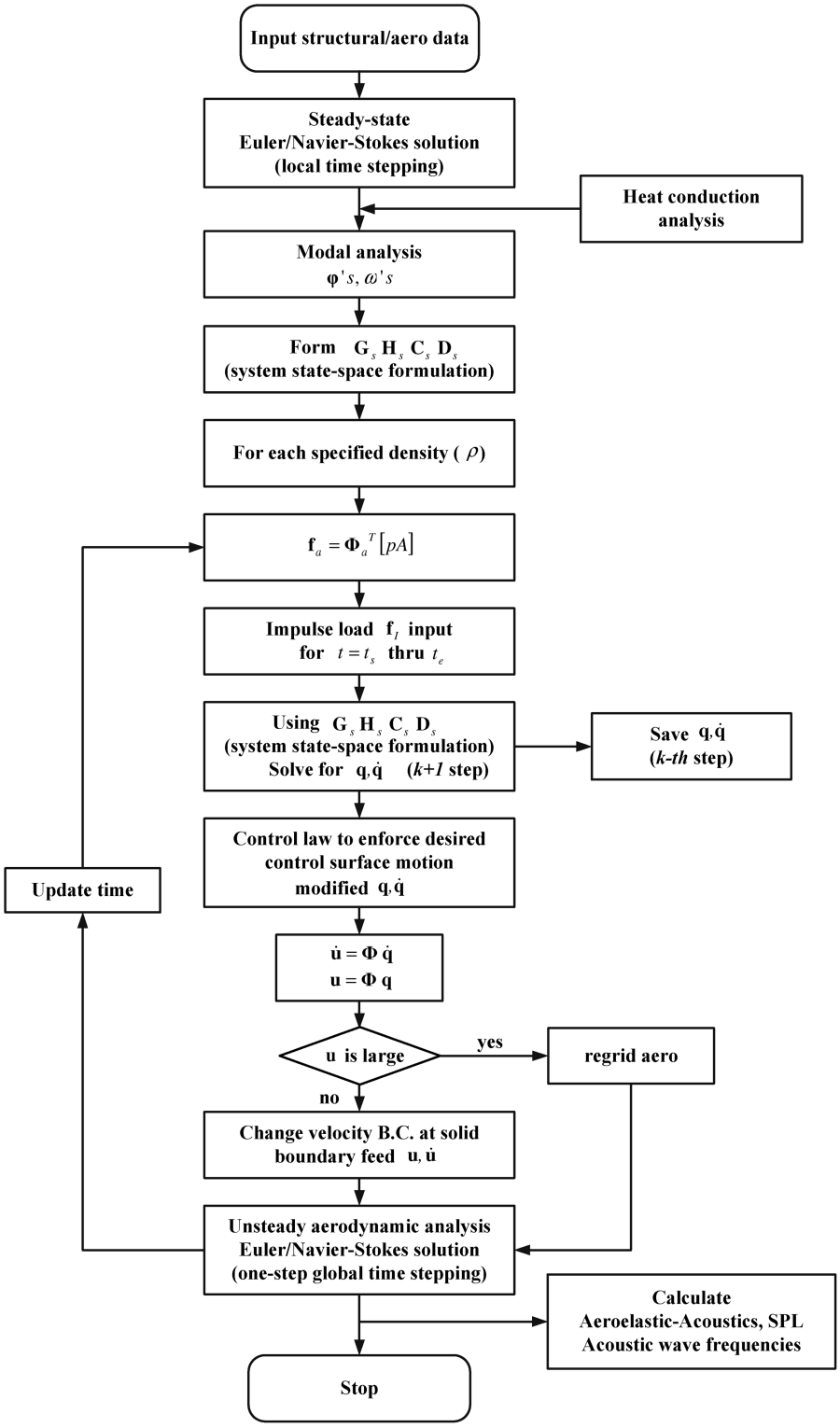

Fig. 1 Aeroelastic-servo–acoustic analysis flowchart. (B.C. denotes the boundary condition.)

distributions that are in turn used for calculation of acoustic field parameters such as wave frequencies and structural-surface sound pressure levels. This analysis procedure starts with an FE structural modeling, followed by a free-vibration analysis that computes the natural frequencies ω and modes $\boldsymbol{\varphi}$ by solving the matrix equation:

$$\boldsymbol{M}\ddot{\boldsymbol{u}} + \boldsymbol{K}\boldsymbol{u} = 0 \tag{1}$$

where $\boldsymbol{M}$ and $\boldsymbol{K}$ are, respectively, the inertia and stiffness matrices of order N, and $\boldsymbol{u}$ is the displacement vector. A steady-state fluid flow solution is next derived using a two-step solution [12] procedure and local time-stepping; this is accomplished by solving the Navier–Stokes equation in conservation form as shown next:

$$\frac{\partial \boldsymbol{v}}{\partial t} + \frac{\partial \boldsymbol{f}_j}{\partial x_j} + \frac{\partial \boldsymbol{g}_j}{\partial x_j} = \boldsymbol{f}_b \qquad j = 1, 2, 3 \tag{2}$$

where $\boldsymbol{f}_i$ and $\boldsymbol{g}_i$ are flow vector convection and diffusion terms, respectively; $\boldsymbol{f}_b$ is the body force vector; and the conservation variables are defined as

$$\boldsymbol{v} = [\rho \quad \rho u_i \quad \rho E]^T \qquad i = 1, 2, 3$$

where ρ, u, and E are the density, velocity, and total energy, respectively. Once the aerodynamic parameters are calculated, the vehicle equation of motion is then cast in the frequency domain, using NR number of modes as shown next:

$$\hat{\boldsymbol{M}}\,\ddot{\boldsymbol{q}} + \hat{\boldsymbol{C}}\,\dot{\boldsymbol{q}} + \hat{\boldsymbol{K}}\boldsymbol{q} + \boldsymbol{f}_a(t) + \boldsymbol{f}_I(t) = 0 \tag{3}$$

where $\boldsymbol{q}$ is the generalized displacement vector ($\Phi^T\boldsymbol{u}$), $\hat{\boldsymbol{M}}$ is the associated generalized inertial matrix ($\Phi^T\boldsymbol{M}\Phi$) of order ($NR \times NR$) and similar transformation is adopted for the stiffness $\hat{\boldsymbol{K}}$ and damping $\hat{\boldsymbol{C}}$ matrices, $\boldsymbol{f}_a(t)$ is the aerodynamic load vector ($\Phi_a^T pA$), p is the fluid pressure at a fluid node (where A is the effective surface area around the node and Φ_a is the modal vector at fluid grid points on the vehicle structural surface), and $\boldsymbol{f}_I(t)$ is the generalized structural impulse force vector.

Equation (3) may then be cast in a state-space matrix form as

$$\begin{bmatrix} \boldsymbol{I} & 0 \\ 0 & \boldsymbol{I} \end{bmatrix}\begin{bmatrix} \dot{\boldsymbol{q}} \\ \ddot{\boldsymbol{q}} \end{bmatrix} - \begin{bmatrix} 0 & \boldsymbol{I} \\ -\hat{\boldsymbol{M}}^{-1}\hat{\boldsymbol{K}} & -\hat{\boldsymbol{M}}^{-1}\hat{\boldsymbol{C}} \end{bmatrix}\begin{bmatrix} \boldsymbol{q} \\ \dot{\boldsymbol{q}} \end{bmatrix} - \begin{bmatrix} 0 \\ -\hat{\boldsymbol{M}}^{-1}\boldsymbol{f}_a(t) \end{bmatrix} - \begin{bmatrix} 0 \\ -\hat{\boldsymbol{M}}^{-1}\boldsymbol{f}_I(t) \end{bmatrix} = 0 \tag{4}$$

or

$$\dot{\boldsymbol{x}}_s(t) = \boldsymbol{A}_{st}\boldsymbol{x}_s(t) + \boldsymbol{B}_{st}\boldsymbol{f}(t) \tag{5}$$

where

$$\boldsymbol{A}_{st} = \begin{bmatrix} 0 & \boldsymbol{I} \\ -\hat{\boldsymbol{M}}^{-1}\hat{\boldsymbol{K}} & -\hat{\boldsymbol{M}}^{-1}\hat{\boldsymbol{C}} \end{bmatrix}, \qquad \boldsymbol{B}_{st} = \begin{bmatrix} 0 \\ -\hat{\boldsymbol{M}}^{-1} \end{bmatrix}$$
$$\boldsymbol{f}(t) = \boldsymbol{f}_a(t) + \boldsymbol{f}_I(t), \qquad \boldsymbol{x}_s = \begin{bmatrix} \boldsymbol{q} \\ \dot{\boldsymbol{q}} \end{bmatrix} \tag{6}$$

and

$$\boldsymbol{y}_s(t) = \boldsymbol{C}_{st}\boldsymbol{x}_s(t) + \boldsymbol{D}_{st}\boldsymbol{f}(t) \tag{7}$$

where $\boldsymbol{C}_{st} = \boldsymbol{I}$, $\boldsymbol{D}_{st} = 0$, matrix $\boldsymbol{A}_{st}$ is of order $NR2 \times NR2$ ($NR2 = 2 \times NR$), and $\boldsymbol{B}_{st}$ is a $NR2 \times NR$ matrix.

In the presence of sensors, their motions can be expressed relative to the generalized terms as

$$\begin{Bmatrix} \mathbf{q}(t) \\ \dot{\mathbf{q}}(t) \\ \mathbf{u}_{sn}(t) \\ \dot{\mathbf{u}}_{sn}(t) \\ \ddot{\mathbf{u}}_{sn}(t) \end{Bmatrix} = \begin{bmatrix} \mathbf{I} & \mathbf{0} \\ \mathbf{0} & \mathbf{I} \\ \mathbf{T}_{sn}\Phi & \mathbf{0} \\ \mathbf{0} & \mathbf{T}_{sn}\Phi \\ -\mathbf{T}_{sn}\Phi\hat{\mathbf{M}}^{-1}\hat{\mathbf{K}} & -\mathbf{T}_{sn}\Phi\hat{\mathbf{M}}^{-1}\hat{\mathbf{C}} \end{bmatrix}\begin{Bmatrix} \mathbf{q}(t) \\ \dot{\mathbf{q}}(t) \end{Bmatrix} + \begin{Bmatrix} \mathbf{0} \\ \mathbf{0} \\ \mathbf{0} \\ \mathbf{0} \\ -\mathbf{T}_{sn}\Phi\hat{\mathbf{M}}^{-1} \end{Bmatrix}\mathbf{f}(t) \tag{8}$$

or

$$\boldsymbol{y}_{ss}(t) = \boldsymbol{C}_{ss}\boldsymbol{x}_s(t) + \boldsymbol{D}_{ss}\boldsymbol{f}(t) \tag{9}$$

where u_{sn} denote the real physical displacements of the sensors in the continuous-time domain. Further, the interpolation matrix T_{sn}, having sensor location information, is of dimensions ($2 \times NS$, N), where NS is the number of sensors. Equation (9) is the sensor output relationship signifying motion at the sensors resulting from the body motion $\boldsymbol{C}_{ss}$ and control motion D_{ss}. Converting the equations from inertial to body-axis frame results in

$$\boldsymbol{x}_s(t) = \tilde{\boldsymbol{T}}_2^{-1}(\boldsymbol{A}_{st}\tilde{\boldsymbol{T}}_1 - \tilde{\boldsymbol{T}}_3)\boldsymbol{x}_s(t) + \tilde{\boldsymbol{T}}_2^{-1}\boldsymbol{B}_{st}\boldsymbol{f}(t) \tag{10}$$

$$\boldsymbol{y}_s(t) = \boldsymbol{C}_{ss}\tilde{\boldsymbol{T}}_1\boldsymbol{x}_s(t) + \boldsymbol{D}_{ss}\boldsymbol{f}(t) \tag{11}$$

which can be written as

$$\boldsymbol{x}_s(t) = \boldsymbol{A}_s\boldsymbol{x}_s(t) + \boldsymbol{B}_s\boldsymbol{f}(t) \tag{12}$$

$$\boldsymbol{y}_s(t) = \boldsymbol{C}_s\boldsymbol{x}_s(t) + \boldsymbol{D}_s\boldsymbol{f}(t) \tag{13}$$

where $\tilde{\boldsymbol{T}}_1$, $\tilde{\boldsymbol{T}}_2$, and $\tilde{\boldsymbol{T}}_3$ are coordinate transformation matrices of dimension ($NR2 \times NR2$). These equations, representing the most general aeroservoelastic (ASE) case, are converted [12] to the zero-order hold discrete-time equivalent at the kth step:

$$\boldsymbol{x}_s(k+1) = \boldsymbol{G}_s\boldsymbol{x}_s(k) + \boldsymbol{H}_s\boldsymbol{f}(k) \tag{14}$$

$$\boldsymbol{y}_s(k+1) = \boldsymbol{C}_s\boldsymbol{x}_s(k) + \boldsymbol{D}_s\boldsymbol{f}(k) \tag{15}$$

where

$$\boldsymbol{f}(k) = \boldsymbol{f}_a(k) + \boldsymbol{f}_I(k) \tag{16}$$

$$\boldsymbol{G}_s = e^{\boldsymbol{A}_s\Delta t}, \qquad \boldsymbol{H}_s = [e^{\boldsymbol{A}_s\Delta t} - \boldsymbol{I}][\boldsymbol{A}_s^{-1}\boldsymbol{B}_s] \tag{17}$$

$\Delta t = t_{k+1} - t_k$, and $\boldsymbol{C}_s$ and $\boldsymbol{D}_s$ remain unaltered.

Sound is defined as any disturbance that travels through an elastic media such as air, ground, or water at a speed of 340 m/s in air at sea level, and it is considered to be oscillations that flow transversely or outwardly in straight lines in the form of pressure waves. These flows that travel at the speed of sound define acoustic waves.

Figure 1 depicts the analysis flowchart for the general AE/ASE analysis with acoustic simulation. Once the unsteady pressures are computed, the sound pressure level (SPL) for a specified node is calculated by first fixing a time band ($t = t_j$) and then computing the root mean square (rms) of unsteady pressure. The standard calculations using n number of sampling points are as follows:

1) Compute average pressure:

$$P_{\text{avg}} = \frac{\left(\sum_{i=1}^{n} P_i\right)}{n} \tag{18}$$

2) Compute the root mean square of pressure:

$$P_{\text{rms}} = \sqrt{\frac{\sum_{i=1}^{n}(P_i - P_{\text{avg}})^2}{n}} \tag{19}$$

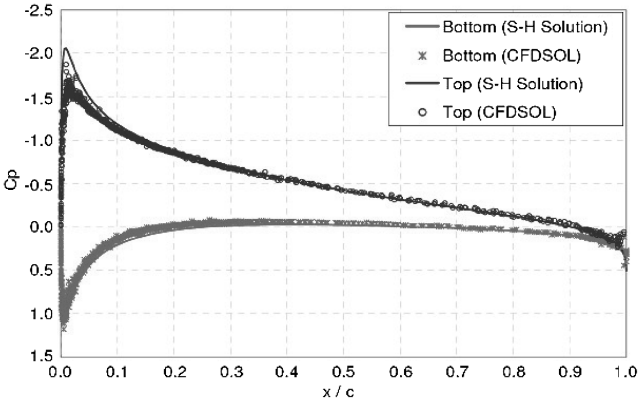

Fig. 2 C_p distribution on the airfoil. (S-H denotes Smith–Hess.)

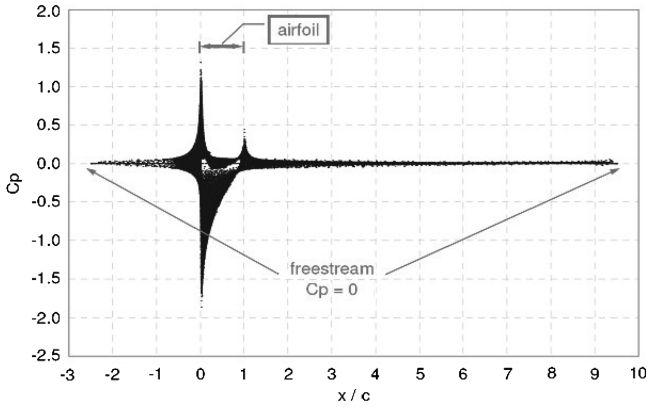

Fig. 3 C_p distribution over the solution domain.

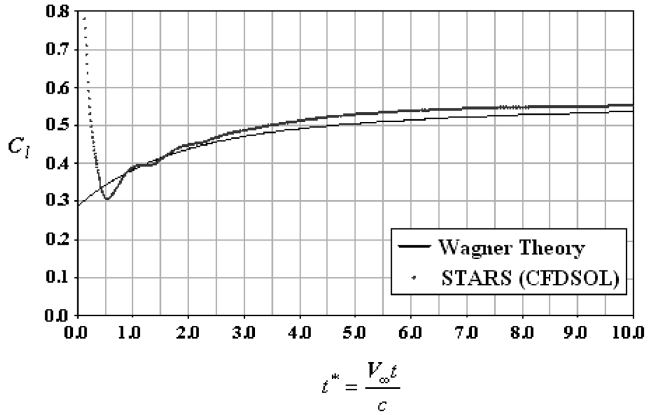

Fig. 4 Unsteady C_l history.

3) Compute the sound pressure level:

$$\text{SPL (dB)} = 20\log_{10}\frac{P_{\text{rms}}}{P_{\text{ref}}} \tag{20}$$

The reference pressure $P_{\text{ref}} = 20 \times 10^{-6}$ Pa for air. Further, nodal temperature T distribution on the wing structure is calculated from enthalpy H as

$$T = \frac{H}{c_p} \tag{21}$$

where c_p is specific heat capacity at constant pressure. As depicted in Fig. 1, thermal effects may need to be taken into consideration if they modify the modal solution significantly, which will in turn affect the unsteady pressure and, hence, the acoustic calculations.

Similarly, the acoustic-wave frequencies are derived by performing fast Fourier transform (FFT) on the unsteady pressure data:

$$\text{FFT}\,(P_{\text{unstd}}, t) = F(\omega) \qquad \text{PSD} = \frac{F(\omega) \times F(\omega)^*}{2\Delta f} = \frac{|F(\omega)|^2}{2\Delta f}$$

$$\Delta f = \frac{1}{t_j} \tag{22}$$

PSD is the power spectral density. Acoustic-wave frequencies and amplitudes are obtained from the peaks of the plotted curves.

III. Numerical Examples

In an effort to verify the solution accuracy for the STARS CFD module and for subsequent aeroelastic-acoustics simulation, a simple NACA 0012 airfoil was chosen for steady and unsteady flow analyses with known theoretical solutions. Subsequently, a 3-D cantilever wing with a NACA 0012 airfoil was analyzed for computation of acoustic outputs, which are presented herein in some

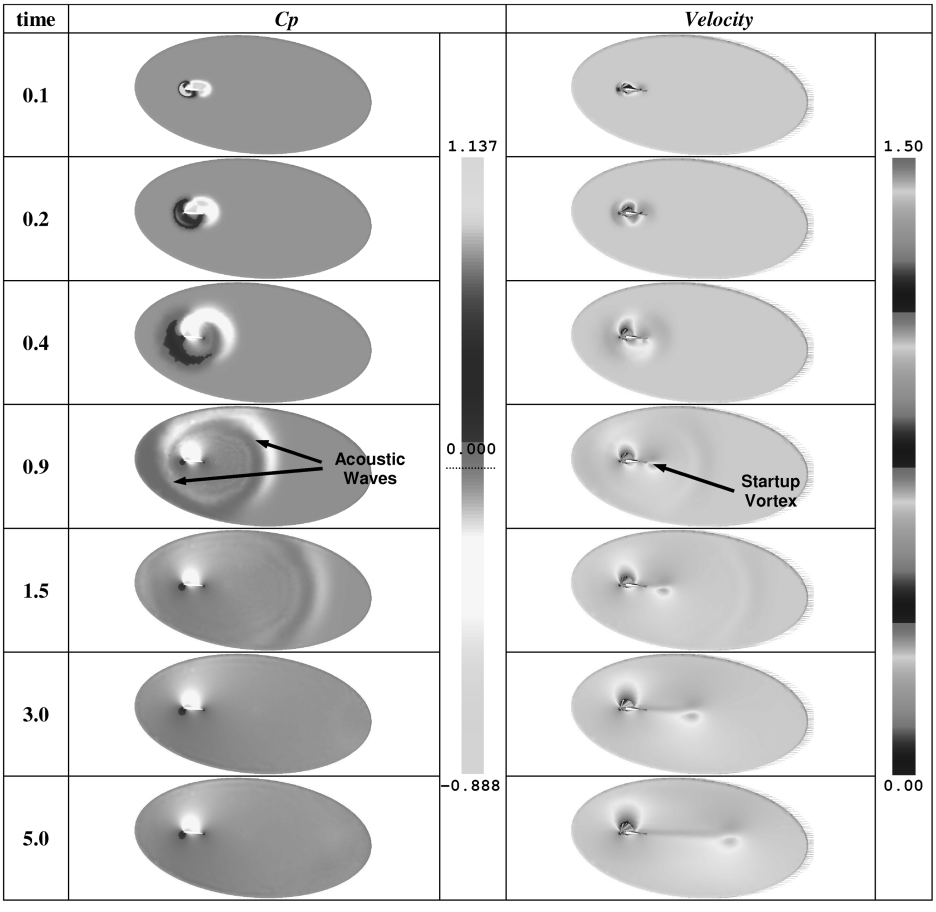

Fig. 5 Unsteady analysis of C_p and velocity distribution.

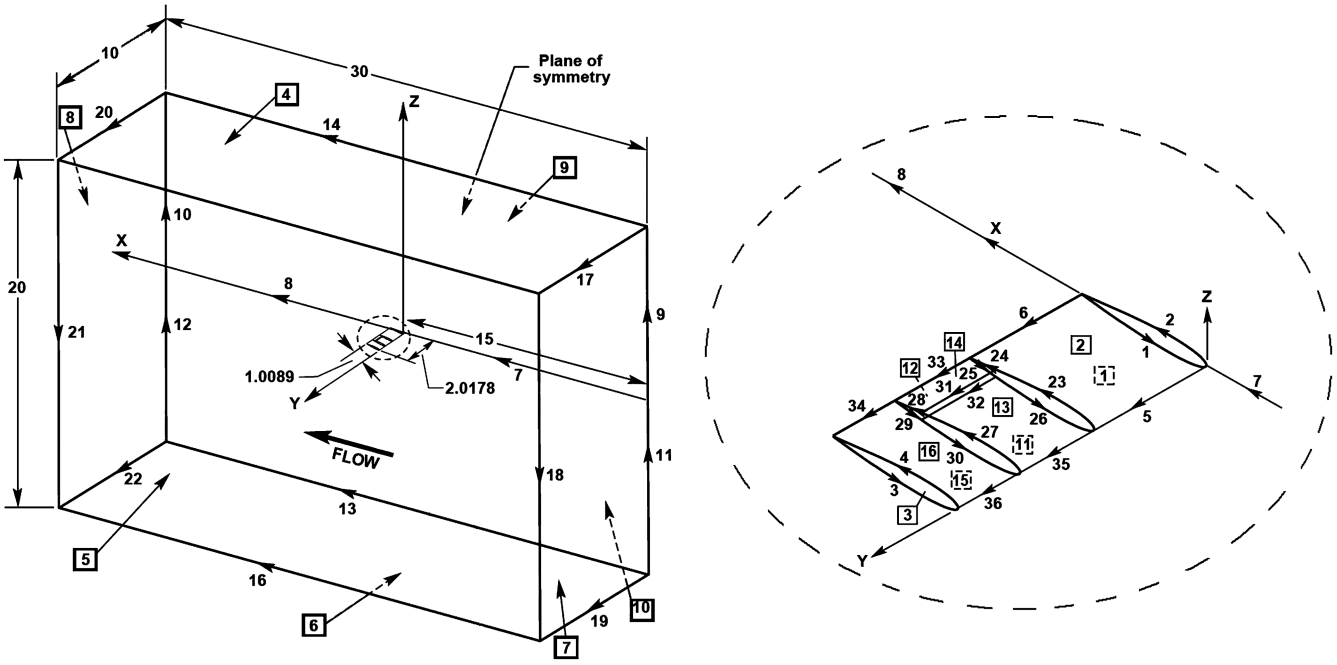

Fig. 6 Cantilever wing with aeroelastic solution domain.

detail, depicting such a simulation capability with large-scale finite element software that is suitable for analysis of complex practical problems. The analysis process (Fig. 1) starts with a steady-state CFD solution, followed by a structural modal analysis. The resulting aerodynamic and structural dynamic data are then used for the state-space aeroelastic formulation. Next, for each specified flight density, the aeroelastic solutions are effected, yielding the displacement and velocity values. If the displacement values $\boldsymbol{q}$ are moderate, a transpiration boundary condition is applied to the velocity vectors at the solid boundary, which is followed by an unsteady solution, and the process is repeated until solution convergence is achieved. The unsteady aerodynamic pressure values of the converged solution are next used to compute SPLs and acoustic-wave frequencies and amplitudes.

All major computations were performed using a single-processor Intel Xeon E3110 at 3.0 GHz and 3.25 GB memory on a Dell desktop.

A. Two-Dimensional Subsonic NACA 0012 Airfoil

A theoretical flow solution of the airfoil for an airspeed of Mach 0.3 and a 5 deg angle of attack was derived earlier using a Smith–Hess panel method [13] employing 195 panels. The solution yields the velocity in each panel, which may then be used to derive

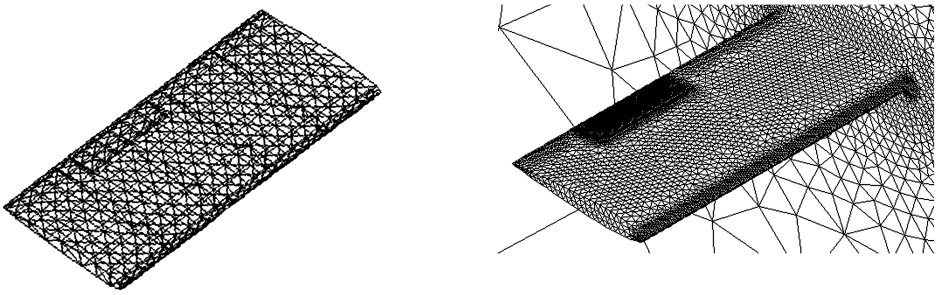

a) The finite element structural mesh of the wing **b) The aerodynamic model of the wing**

Fig. 7 Structural and aerodynamic surface grids of the wing and solution domain.

a) Mode 1, 3.521 Hz., 1B **b) Mode 2, 14.819 Hz., 1T** **c) Mode 7, 59.797 Hz., 1B control**

Fig. 8 Structural modes of the cantilever wing.

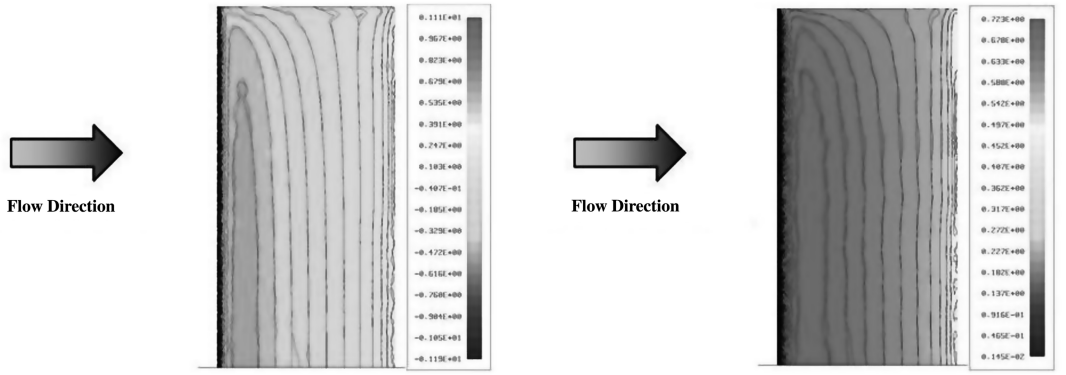

a) Pressure coefficient (C_p) distribution b) Mach number distribution

Fig. 9 Cantilever-wing surface steady-state pressure coefficient and Mach number distribution.

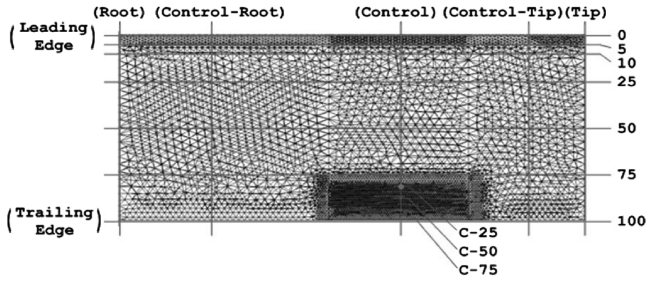

Fig. 10 Layout of the acoustic computation points.

the pressure distribution on the top and bottom surfaces of the airfoil. These pressures can then be converted to coefficient of pressure C_p for comparison purposes and then corrected for compressibility using the standard Prandtl–Glauert subsonic correction formulation. Steady pressure distribution was also computed using the CFDSOL modules of the STARS code, which are then compared in Fig. 2, depicting C_p distribution on the airfoil. Figure 3 shows such a comparison for C_p values through the solution domain; c is the chord length.

The NACA 0012 airfoil was further used to model unsteady flow in the shape of Wagner's suddenly-accelerated-airfoil problem [14].

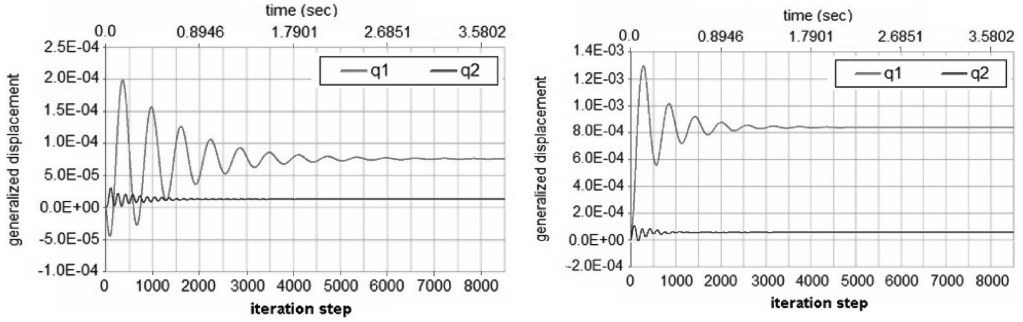

a) Mach 0.3 b) Mach 0.6

Fig. 11 Typical aeroelastic response plot.

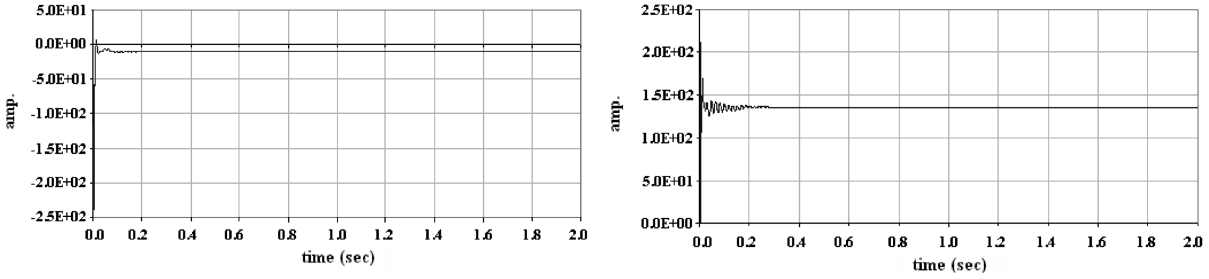

a) Mach 0.3 b) Mach 0.6

Fig. 12 Unsteady aerodynamic pressure plot at node C-25.

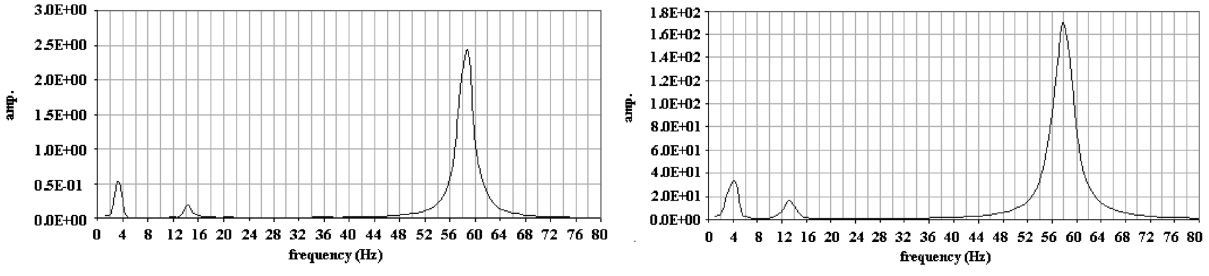

a) Mach 0.3 b) Mach 0.6

Fig. 13 Aeroelastic-acoustic response.

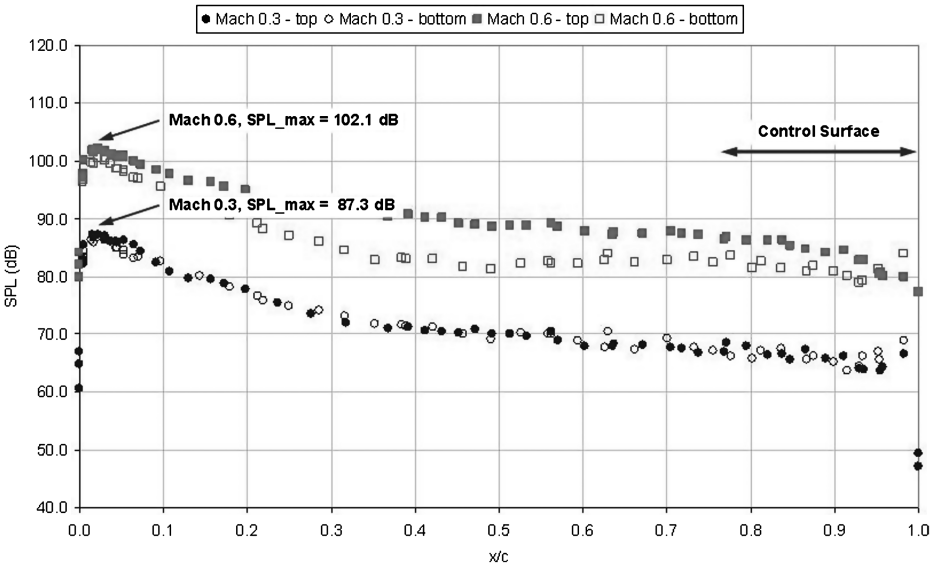

Fig. 14 SPL for a line along the chord length at the control tip.

a) SOFIA aircraft with closed cavity door

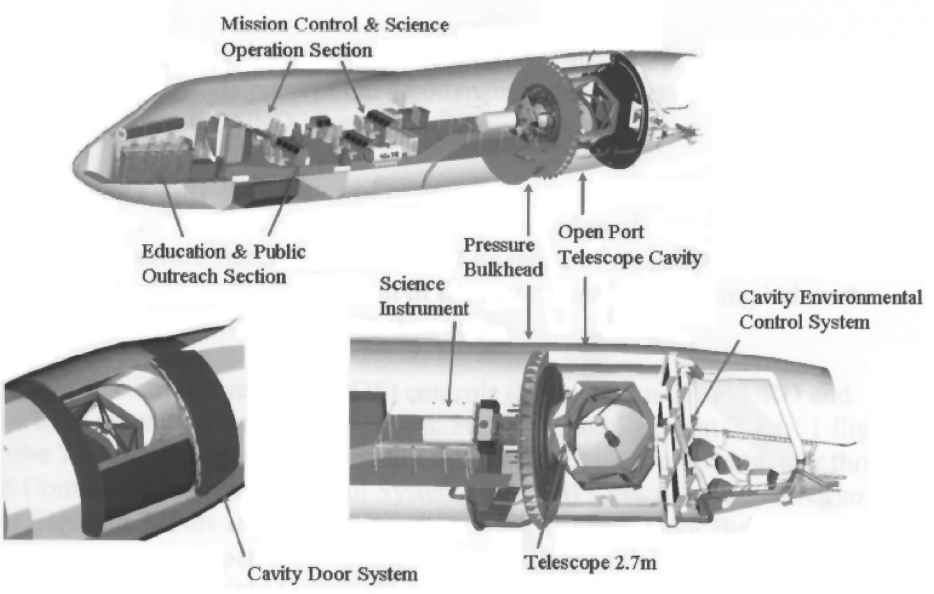

b) SOFIA CAD model

Fig. 15 SOFIA aircraft and a CAD model.

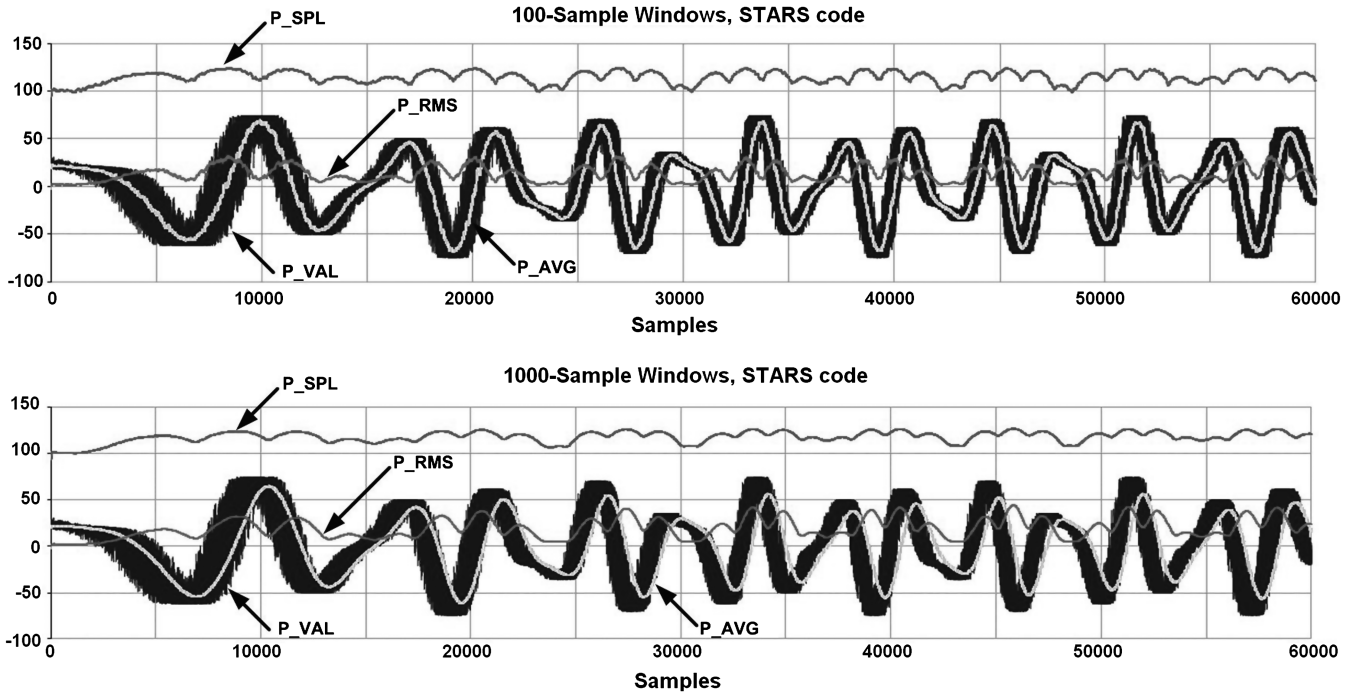

Fig. 16 Simulated pressure data with associated calculation results (SI units).

Unsteady solution results from the CFDSOL are shown in Figs. 4 and 5. Such analysis results were also performed for an airspeed of Mach 0.3 and a 5 deg angle of attack.

The correlation of results between computed values and the test cases for both steady and unsteady flows is remarkably good. Further results depicted in Fig. 5 are obviously related to that shown in Fig. 2. These results have further been correlated with the independent computer code Euler3D, developed by Oklahoma State University [15].

B. Three-Dimensional Cantilever Wing

The cantilever wing [8] with a NACA 0012 symmetric airfoil chosen for the acoustic analysis is more representative of a practical problem and is shown in Fig. 6; all dimensions are in SI units. The structural and aerodynamic grids are shown in Fig. 7. The structural model consists of shell, primarily aluminum, and line elements consisting of ribs and spars. The first few structural modes are shown in Fig. 8; this analysis was performed with a well-established progressive simultaneous iteration algorithm [12]. For the subsequent analyses, modes 1, 2, and 7 were taken into consideration; such modes were originally chosen to induce eventual aeroelastic instability [8]. A typical steady-state CFD solution for Mach 0.6 is depicted in Fig. 9; the solution pertains to either the top or bottom surface as a symmetric airfoil. A layout of the acoustic computation points is shown in Fig. 10. Typical aeroelastic responses such as the generalized displacements $\boldsymbol{q}1$ and $\boldsymbol{q}2$ are shown in Fig. 11 for Mach 0.3 and 0.6, respectively. Similarly, an unsteady pressure distribution at a typical node is shown in Fig. 12. FFT is performed on the unsteady pressure data using a derived sampling rate of around 2200 samples/second to yield an aeroelastic-acoustic response, and associated modes are depicted in Fig. 13; the three modes recorded are around 4.4, 13.1, and 59.7 Hz, respectively. Figure 14 shows the details of data (in decibels) for a line along the chord length.

Major solution CPU times were 3.4 s for structural free-vibration analysis and 20.8 min for the steady-state CFD solution with 1.0E − 8 residuals; corresponding unsteady solution time was 35.4 h for 4000 iterations for the Mach 0.3 case.

C. SOFIA Flight-Test Acoustics Evaluation

Kunz [5] provides details of the SOFIA aircraft and design specification (Fig. 15). During the impending flight test, the aircraft [5] and, particularly, its cavity are being heavily instrumented with pressure gauges, accelerometers, and strain gauges, all at a 500-sample/second minimum for real-time measurements. The tests will involve a combination of Mach numbers and altitudes known as the flight-envelope expansion. The primary frequency domain of concern

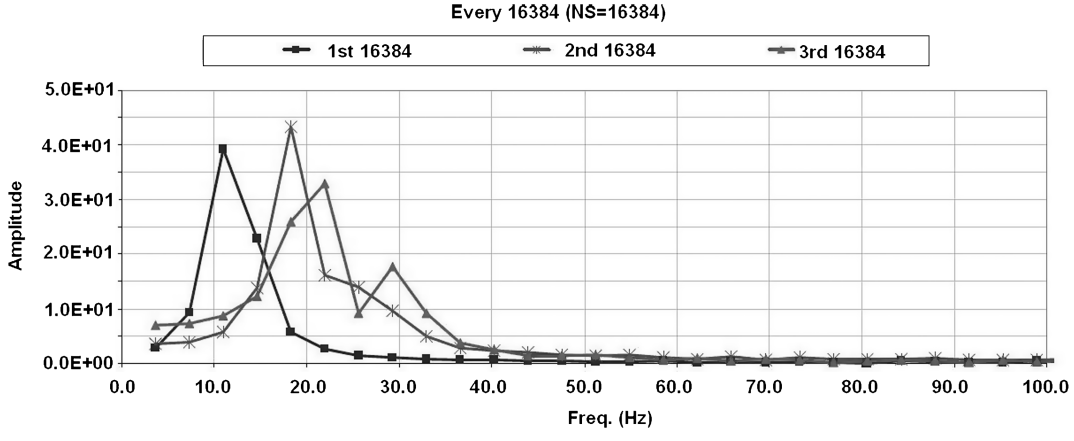

Fig. 17 Typical FFT result showing acoustic-wave frequencies and amplitudes.

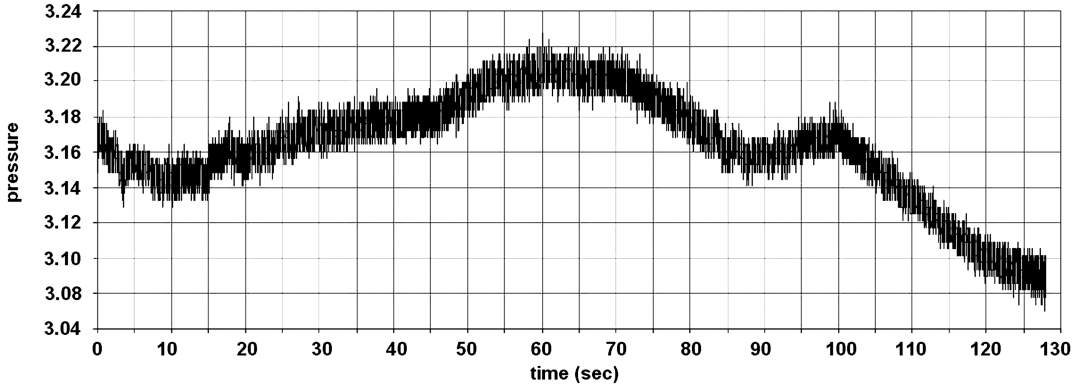

Fig. 18 SOFIA-sensor-measured unsteady pressure data.

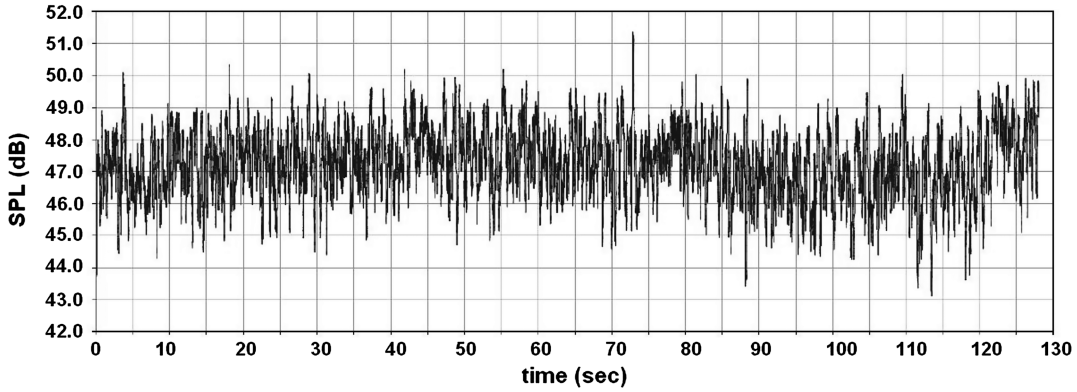

Fig. 19 SOFIA-calculated SPL results data.

is 100 Hz, and the instrumentation is expected to be accurate up to 200 Hz. Real-time data monitoring is of critical importance to detect the advent of any coupling of cavity acoustics and Rossiter modes, which may cause very-high-amplitude acoustic response with debilitating effect on the telescope assembly and the fuselage. Real-time sampling of the unsteady aerodynamic data read by the pressure sensors will enable continued monitoring of acoustic SPLs to be calculated by adapting the analysis procedure described in the paper, with a moving time window for the processing of pressure data. This procedure has been hard-wired at the control-room computers, and if the SPL is found to exceed a certain specified value, this will cause a termination of the flight test, ensuring the safety of the aircraft. In an effort to verify the process, a simulated aerodynamic pressure distribution is shown in Fig. 16, along with the average, rms, and SPL distribution. An FFT applied to an unsteady pressure distribution yields the acoustic-wave frequencies and amplitudes, and Fig. 17 shows such a set of results. A typical set of pressure data recorded in a sensor located outside the cavity door of SOFIA aircraft flying at 323 kt at an altitude of 33,000 ft is shown in Fig. 18. Figure 19 depicts the sound pressure level for the data point.

IV. Conclusions

An integrated aeroelastic-acoustics simulation procedure for flight vehicles, among others, is presented in this paper. This novel methodology employs the common finite element techniques for fluids and structures disciplines, using unstructured grids for model idealization. Once the unsteady pressures generated by the interactions of the two disciplines are computed, the acoustics parameters such as wave frequencies and sound pressure levels are calculated by using FFT and the pressure rms values, respectively.

A representative example problem is solved and such results are compared with available theoretical solution data. Numerical accuracy of the current analysis procedure is amply demonstrated in Figs. 2–5. depicting a comparison of present and available solution results. Some detailed analysis results are also presented for a 3-D-wing problem to demonstrate the efficacy of the newly developed analysis process and the associated code. The developed capability is unique in the sense that it enables routine solution of complex practical problems in an accurate fashion. Future effort that includes the effect of temperature on material properties, thereby altering simulation results, will be of much use and importance.

Acknowledgments

Sincere thanks are due to J. Ginsberg of Georgia Institute of Technology and Kevin Knudtsen of NASA Dryden Flight Research Center for their assistance in the preparation of this work.

References

[1] Ko, W. L., and Gong, L., "Thermostructural Analysis of Unconventional Wing Structures of a Hyper-X Hypersonic Flight Research Vehicle for the Mach 7 Mission," NASA TP-2001-210398, 2001.

[2] Gupta, K. K., and Bach, C., "Computational Fluid Dynamics-Based Aeroservoelastic Analysis with Hyper-X Applications," *AIAA Journal*, Vol. 45, No. 7, July 2007, pp. 1459–1471. doi:10.2514/1.21992

[3] Pendleton, E., "Active Aeroelastic Wing," *AFRL Technology Horizons*, Vol. 1, No. 2, June 2000, pp. 27–28.

[4] Gupta, K. K., and Bach, C., "System Identification Approach for a Computational-Fluid-Dynamics-Based Aeroelastic Analysis," *AIAA Journal*, Vol. 45, No. 12, Dec. 2007, pp. 28202827. doi:10.2514/1.28647

[5] Kunz, N., "The SOFIA Aircraft and its Modification," *Airborne Telescope Systems II*, Proceedings of SPIE, Vol. 4857, SPIE, Bellingham, WA, pp. 333–343, 2003.

[6] Srinivasan, G. R., and Klotz, S. P., "Features of Cavity Flow and Acoustics of the Stratospheric Observatory for Infrared Astronomy," ASME Fluids Engineering Conference, American Society of Mechanical Engineers, Paper 97-3647, Fairfield, NJ, June 1997.

[7] McIntyre, M., "Analysis of SOFIA Cavity Acoustic Modes," Stratospheric Observatory for Infrared Astronomy, TN MJM-011, 2000.

[8] Gupta, K. K., "STARS: An Integrated General-Purpose Finite Element Structure, Aeroelastic and Aeroservoelastic Analysis Computer

Program," NASA TM-4795, May 1997 (Rev. Sept. 2006).
[9] Lighthill, M. J., "On Displacement Thickness," *Journal of Fluid Mechanics*, Vol. 4, 1958, pp. 383–392. doi:10.1017/S0022112058000525
[10] Sanker, L. N., Malone, J. B., and Sehuster, D., "Euler Solutions for Transonic Flow Past a Fighter Wing," *Journal of Aircraft*, Vol. 24, No. 1, 1987, pp. 10–16. doi:10.2514/3.45404
[11] Stephens, C. H., Arena, A. S., and Gupta, K. K., "Application of Transpiration Method for Aeroelastic Prediction Using CFD," AIAA Paper 98-2071, April 1998.
[12] Gupta, K. K., and Meek, J. L., *Finite Element Multidisciplinary Analysis*, 2nd ed., AIAA Education Series, AIAA, Reston, VA, Sept. 2003.
[13] Hess, J. L., and Smith, A. M. O., "Calculation of Potential Flow About Arbitrary Bodies," *Progress in Aeronautical Sciences*, Vol. 8, 1967, pp. 1–138. doi:10.1016/0376-0421(67)90003-6
[14] Wagner, H., "Uber die Entstehung des dynamischen Auftriebes von Tragflugeln," *Zeitschrift fur Angewandte Mathematik und Mechanick*, Vol. 5, No. 1, 1925, pp. 17–35. doi:10.1002/zamm.19250050103.
[15] Stephens, C. H., and Arena, A., "CFD-Based Aeroservoelastic Predictions with Comparisons to Benchmark Experimental Data," AIAA Paper 99-0766, Jan. 1999.

A. Sinha
Associate Editor